Nanoscale Advances

ROYAL SOCIETY OF CHEMISTRY

PAPER

View Article Online
View Journal | View Issue



Cite this: *Nanoscale Adv.*, 2021, **3**, 1136

# Flexible MnO nanoparticle-anchored N-doped porous carbon nanofiber interlayers for superior performance lithium metal anodes†

Jing Yan,‡[a] Min Liu,‡*[ac] Nanping Deng,[b] Liyuan Wang,[d] Alain Sylvestre,[c] Weimin Kang *[a] and Yixia Zhao*[a]

Received 21st August 2020
Accepted 9th December 2020

DOI: 10.1039/d0na00690d

rsc.li/nanoscale-advances

The mounting requirements for electric apparatus and vehicles stimulate the rapid progress of energy storage systems. Lithium (Li) metal is regarded as one of the most prospective anodes for high-performance cells. However, the uneven dendrite growth is one of the primary conundrums that hampers the use of the Li metal anode in rechargeable Li batteries. Achieving even Li deposition is crucial to solve this concern. In this study, a stable interlayer based on electrospun flexible MnO nanoparticle/nitrogen (N)-doped (polyimide) PI-based porous carbon nanofiber (MnO–PCNF) films was effectively prepared *via* electrospinning and *in situ* growth of MnO to reduce the growth of Li dendrites. It is revealed that the attraction of implanted MnO towards Li, the lithiophilic nature of N dopants and the capillary force of porous architectures are beneficial to the preeminent Li wettability of the MnO–PCNF interlayer. Furthermore, the wettable, stable and conductive structure of the MnO–PCNF interlayer can be retained well, offering rapid charge transfer to Li redox reactions, reduced local current density during the cycling process and homogeneous distribution of deposited Li. Consequently, anodes with MnO–PCNF interlayers can relieve the volume change and inhibit the growth of Li dendrites, demonstrating a remarkable lifetime for lithium metal cells at high current.



## 1. Introduction

Lithium (Li) metal is regarded as one of the most hopeful anode candidates for next-generation rechargeable cells due to its high theoretical specific capacity (3860 mA h $g^{-1}$) and lowest electrode potential (−3.04 V).[1] However, challenges brought *via* the uncontainable dendrite growth of the Li metal have seriously restrained its commercial application.[2,3] The uneven Li deposition and Li dendritic growth would not only result in abundant clusters of "dead Li" and low coulombic efficiency (CE), but also lead to short circuit since Li dendrites may pierce the separator, bringing about safety issues.[4–6]

A large number of works has been completed to solve the irrepressible Li dendrite growth. One of the methods is to focus on introducing multiple additives ($LiS_x$ and $LiNO_3$)[7–10] into the electrolyte to improve the surface solid electrolyte interphase (SEI) film,[11,12] and have proved to enhance the formation of uniform SEI films to conquer Li dendrites.[7,13] Another method is to constitute one artificial SEI barrier by depositing various micro/nano-sized materials (*e.g.* hollow carbon nanospheres and oxidized nanofibers) on the Li metal surface.[14–19] More recently, significant attention has been paid to structure a conductive nano-structural interlayer with protective effects for Li metal batteries.[20,21] The growth of Li dendrites at high current densities is mitigated *via* reducing local current densities using conductive interlayers. Common interlayers were composed of improved carbon-based composites that consisted of various carbon materials, reformative polymer-based and metal or inorganic compound-based materials.[22]

Some porous carbon nanofibers (PCNFs) show outstanding mechanical advantage, good structural integrity, remarkable electrical conductivity and large specific surface area,[23] which can accelerate the conduction of Li ions and electrons.[26] Because of these significant advantages, PCNFs are considered hopeful interlayer materials for Li metal anodes.[17,24,27,28] In addition, numerous pores on the PCNF surface serve as active sites for controlling the initial nucleation of Li and generate the capillary force for the Li metal to induce homogeneous lithium

[a]*State Key Laboratory of Separation Membranes and Membrane Processes/National Center for International Joint Research on Separation Membranes, School of Textile Science and Engineering, Tiangong University, Tianjin 300387, China. E-mail: mikeliumin@163.com; kangweimin@tiangong.edu.cn; carlkarl1234@163.com*

[b]*School of Material Science and Engineering, Tiangong University, Tianjin 300387, China*

[c]*University Grenoble Alpes, CNRS, Grenoble INP, G2Elab, 38000 Grenoble, France*

[d]*School of Materials Science and Engineering, Henan Normal University, Xinxiang, Henan, 453007, P. R. China*

† Electronic supplementary information (ESI) available. See DOI: 10.1039/d0na00690d

‡ These authors contributed equally to this work and should be considered cofirst authors.

deposition.[15] Furthermore, the incorporation of N functional groups into PCNFs greatly accelerated the nucleation of Li on PCNFs *via* the significantly reduced nucleation energy barrier.[25] Among miscellaneous fabrication methods of PCNFs, the electrospinning method demonstrates numerous merits such as simple process, versatile structures and low cost for yielding continuous nanofibers.[29]

Common nanostructural interlayer materials such as carbon materials, which do not have very good compatibility with the Li metal, show nucleation overpotential during Li nucleation. Recently, Cui and colleagues have first researched selective lithium deposition *via* heterogeneous seed growth.[30] Using nanomaterials such as gold and silicon dioxide that have zero overpotential of Li nucleation as seeds,[16,28,31,32] the Li metal would selectively nucleate on the seeds and could grow in a controlled manner on anode substrates.[30,33,34] Hence, constructing a lithiophilic interlayer with homogenously distributed Li metal seeds for uniform Li metal growth is rather key for the dendrite-free Li metal anode. Certainly, there is still an imperative requirement to excogitate more interlayers with conductive stable and lithiophilic performances to develop a simpler synthetic process, which manufactures ideal hybrid architectures for improving the electrochemical performance and safety of Li metal anodes at high current.[35]

Herein, we first report the exploration of electrospun flexible MnO nanoparticle/nitrogen (N)-doped polyimide (PI)-based porous carbon nanofiber (MnO–PCNF) films as highly stable interlayers to store Li for dendrite-free Li metal anodes. The PI-based materials were useful for carbon materials to form a stable self-support and flexible architecture, which can simplify the process of battery assembly without any binder,[36] accommodate the Li volume change, and gain a long lifetime of the corresponding electrode.[37] Furthermore, N-doped PI-based carbon nanofibers have been proved to be lithiophilic, and they could induce homogeneous Li deposition.[38,39] MnO can combine with $Li^+$ to generate an analogous alloy reaction during the whole Li deposition–stripping process,[27] and the presence of MnO is useful for carbon materials to form a stable self-support and flexible architecture.[40] The Li metal deposition behaviour on MnO–PCNFs was investigated, and the schematic is shown in Fig. 1. The Li metal is induced to nucleate and grow on the interlayers by MnO–PCNFs. By contrast, uneven Li agglomerates and grows outside of pure CNFs. It is predicted that the synergistic functions of the porous architectures, the lithiophilic N dopants and the embedded MnO nanoparticles can chemically react with Li, which would be significantly conducive to the excellent lithiophilicity of MnO–PCNF interlayers. The porous carbon nanofiber with a large specific surface area and outstanding mechanical strength could not only act well in keeping the structural stability of MnO–PCNF interlayers, but also offer physical confinement of deposited Li and assured rapid electron/ion transport during the Li stripping/plating process. Based on the above-mentioned original designs, the obtained MnO–PCNF composite anodes can deliver long-term cycling stability and small voltage hysteresis at high current.

## 2. Experimental

### 2.1. Fabrication of manganese oxide nanoparticle-doped porous carbon nanofiber films

The precursor solution was prepared as follows: manganese (Mn)-based polyamide acid (PAA) at a concentration of 18% was synthesized by dissolving PMDA, ODA and $MnCl_2$ in DMF under constant stirring for 8 hours. The electrospinning method was conducted under optimized conditions at a flow rate of 0.8 mL $h^{-1}$, a voltage of 25 kV and a tip-collector distance of 20 cm. The Mn-based PAA nanofiber membranes were collected on an aluminum foil. As shown in Fig. 2, the Mn-based PAA membrane was first imidized in a muffle furnace under the following condition: heating up to 100 °C, 200 °C and 300 °C at

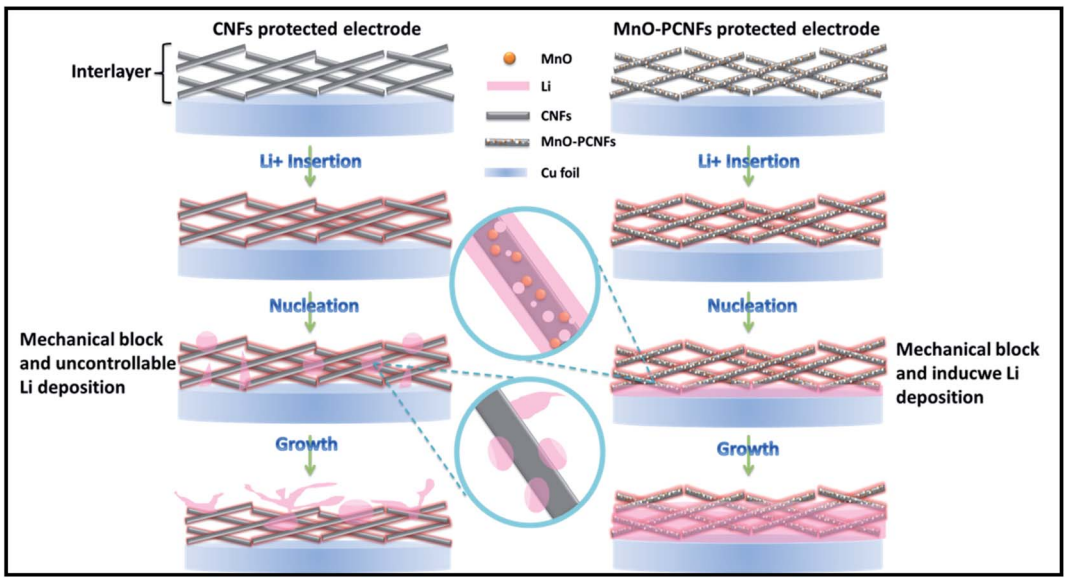


Fig. 1 Schematic of the Li deposition/stripping process of CNFs and MnO–PCNF interlayers.

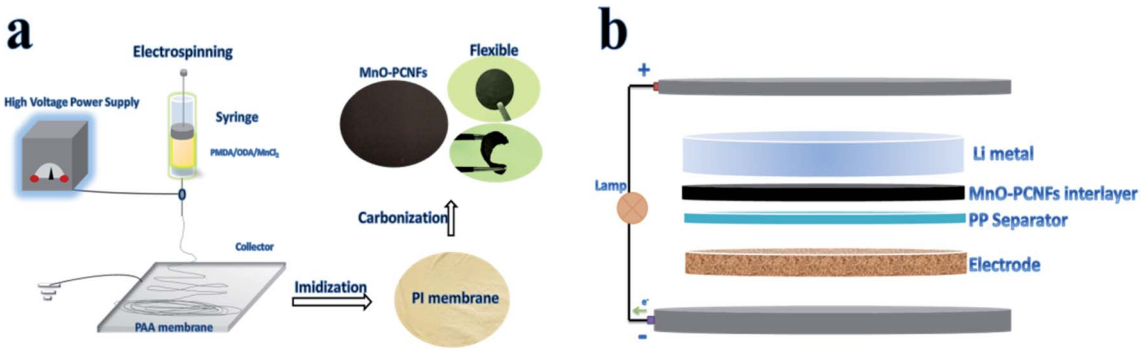


Fig. 2 (a) Schematic of the preparing and packaging process for flexible films. (b) Configuration of a Li–Li (Li–S) cell with a functional flexible MnO–PCNF interlayer.

a rate of 4 °C $min^{-1}$, respectively, followed by a constant temperature craft for 40 min at each former temperature stage. Afterward, the fiber film was carbonated in a nitrogen atmosphere at 800 °C for 1 h to obtain PI-based manganese oxide nanoparticle-doped porous carbon nanofiber (MnO–PCNF) films. PI-based carbon nanofiber films (CNFs) without $MnCl_2$ addition were also prepared by the above-described method.

### 2.2. Electrochemical measurements

The obtained flexible MnO–PCNF films were cut into a circular shape with a diameter of 14 mm; meanwhile, the Li foil was also cut into the same circular shape in an argon-filled glove box. The obtained flexible MnO–PCNF films were measured with an average thickness of 30 μm and an average loading of 0.64 mg $cm^{-2}$ in Fig. 2(a). The weight percentage of MnO in the composite MnO–N-doped carbon fiber film was 24.30% according to the weight fraction of the elements given in Table S2.†

For all cells, electrochemical characterizations were performed using assembled CR2340-type coin cells, as shown in Fig. 2(b). The samples of the obtained flexible CNF films were prepared *via* the same route as the obtained flexible MnO–PCNF films. The Li metal foil, PP, MnO–PCNF films and the Cu metal foil were assembled in Li–Cu cells. Two Li metal foils with MnO–PCNF films were assembled as the working and counter electrodes in symmetrical cells. The sulfur cathode with a sulfur loading of 1.26 mg $cm^{-2}$, PP, MnO–PCNF films and the Li metal foil were employed in the Li–S cells.

## 3. Results and discussion

### 3.1 Morphological structures

The microstructures and morphologies of the obtained flexible PI-based CNFs with 5% $MnCl_2$ at 600, 800 and 1000 °C were

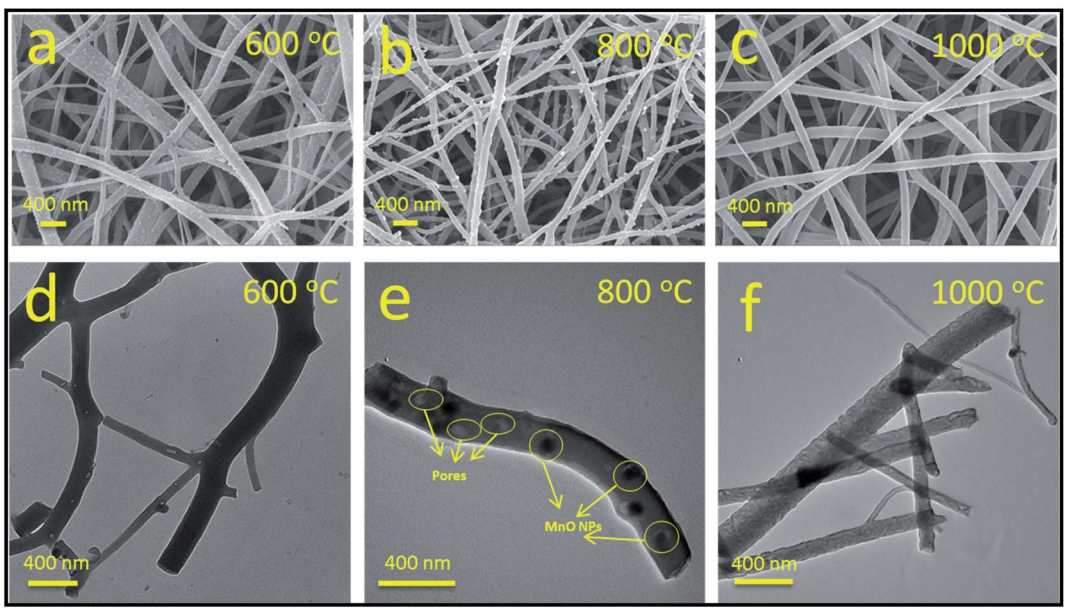


Fig. 3 SEM images of PCNFs added with 5 wt% $MnCl_2$ at (a) 600 °C, (b) 800 °C and (c) 1000 °C. TEM images of PCNFs added with 5 wt% $MnCl_2$ at (d) 600 °C, (e) 800 °C and (f) 1000 °C.

studied by SEM and TEM, as presented in Fig. 3(a–f). As demonstrated in Fig. 3(a and d), the typical carbon architecture of flexible PI-based PCNFs with $MnCl_2$ can be obtained in as-spun nanofibers after the preoxidation and carbonization procedure. The porous morphological architecture of pure PCNFs was not obvious.[41] As demonstrated in Fig. 3(b and e), the porous structures of the obtained pure PCNFs at both 800 and 1000 °C were obvious, which could accommodate the volume expansion of the Li metal and accelerate lithium insertion into the interior/surface of the prepared carbon nanofibers. In addition, various fine MnO nanoparticles were observed in PCNFs, and the particle diameter was less than 100 nm. The morphological architectures of PCNFs at 1000 °C are displayed in Fig. 3(c and f). Because of the high temperature, MnO nanoparticles were not observed, as they were decomposed when the temperature reached 1000 °C. Furthermore, the electrical conductivity of MnO–PCNFs at 600 °C was lower than that at 800 °C because of the low degree of graphitization. In addition, the flexibility of MnO–PCNFs at 1000 °C was not better than that at 800 °C due to the high degree of carbonation. Therefore, 800 °C was chosen as the optimal temperature among them: the size of the Mn-based particles was medium, and a certain scale was maintained with the carbon fiber, so that the bond between the carbon fiber and the MnO particles was strong. The MnO particles of flexible electrospun porous carbon nanofiber structures could offer more active sites to induce more abundant and uniform Li deposition and stripping.[15,16] Fig. 4(b) displays the morphological architecture of flexible PI-based MnO–PCNFs, showing that the MnO nanoparticle architecture can be formed in flexible PCNFs. The prepared MnO nanoparticles of homogeneous size were uniformly distributed on flexible PCNFs.

The capillary force of the porous architectures is conducive to the great Li wettability of flexible MnO–PCNFs,[15,17] which makes it easier for Li to catch the growth sites during the deposition process and deposit them on the structure of PCNFs in an orderly manner.[34,42] In the procedure, the MnO Nanoparticles (NPs) can be homogeneously manufactured on flexible PCNFs by the *in situ* synthesis procedure. During the carbonization method, the high temperature enabled a tough combination between MnO NPs and PCNFs. The prepared MnO NPs in PCNFs were homogeneously dispersed on the surface of PCNFs. To precisely verify the distribution of MnO NPs in the skeleton of PCNFs, energy-dispersive X-ray (EDX) spectroscopy was implemented to probe the distribution of chemical elements for flexible MnO–PCNFs. Fig. 4(d) presents the EDS mapping image of flexible PI-based MnO–PCNFs. The Mn element was homogeneously distributed in flexible MnO–PCNFs, which proved the uniform distribution of MnO particles in flexible MnO–PCNFs.

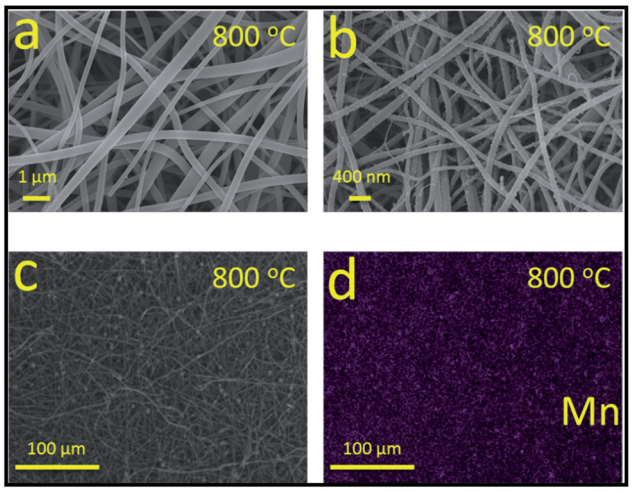


Fig. 4 (a) SEM images of PCNFs at 800 °C. (b) TEM images of PCNFs added with 5 wt% $MnCl_2$ at 800 °C. (c) SEM image of MnO–PCNFs and (d) its corresponding EDX elemental mapping image of Mn.

### 3.2 Spectroscopic analysis and thermo gravimetric analysis

To classify the crystal architecture of the as-obtained flexible CNF and MnO–PCNF composites, the XRD of the composites was examined, as shown in Fig. 5(a). The XRD spectrum of flexible CNFs displayed a wide diffraction peak at 26.4°. The diffraction peaks of flexible MnO–PCNF composites at 34.9°, 41.0°, 58.7°, 70.1°, 73.8° and 87.7° were indexed to the (111), (200), (220), (311), (222) and (400) planes, corresponding to the manganosite phase of MnO (PDF 75-1090), respectively.[43,44] The broadening diffraction peaks showed that the small grain size with a nano-scale can be obtained for the as-decorated MnO NPs. The size of MnO was assessed *via* applying the Debye–Scherrer equation to the (111) peak. The outcomes showed that $MnCl_2$ had been effectively changed into MnO. On the Mn 2p spectra (Fig. 5(b)), the disparity between Mn $2p_{1/2}$ and Mn $2p_{3/2}$ was 11.6 eV, approving with the feature of MnO, corresponding to the XRD consequences.[44] The high-resolution XPS spectra of the N 1s peak (Fig. 5(c)) could be divided into three fitting peaks located at 398.4, 399.6 and 400.6 eV, corresponding to pyridinic N, pyrrolic N, and quaternary N, respectively. The incorporation of N effective groups greatly accelerated the nucleation of Li on PCNFs based on the largely reduced nucleation energy barrier.[25] The structure of the existing MnO and the N co-doped carbon nanofibers could be regarded not only as a Li reservoir to allow the electrode level stability, but also as a composite current collector to regulate the initial nucleation and following growth of Li.[45] The thermal properties of MnO–PCNF composites were evaluated by TGA, and the obtained results are displayed in Fig. 5(d). From the TGA curves, it could be observed that a minor weight loss happened from 50 °C to 150 °C in the MnO–PCNF sample, which was because of the removal of dampness and scums. The weight of MnO–PCNF samples decreased gradually from 200 °C to 400 °C, which could be because of the imidization process of PAA to PI and the preparation of MnO. In the process, water molecules were formed. During 450 °C to 800 °C, the loss of mass was owing to the carbonation of PI, in which $CO_2$ and water molecules were produced.[43] The slight decrease in the temperature range of 880–900 °C could be due to the reduction of MnO into Mn, in which there was $CO_2$ creation in the procedure.[25,32]

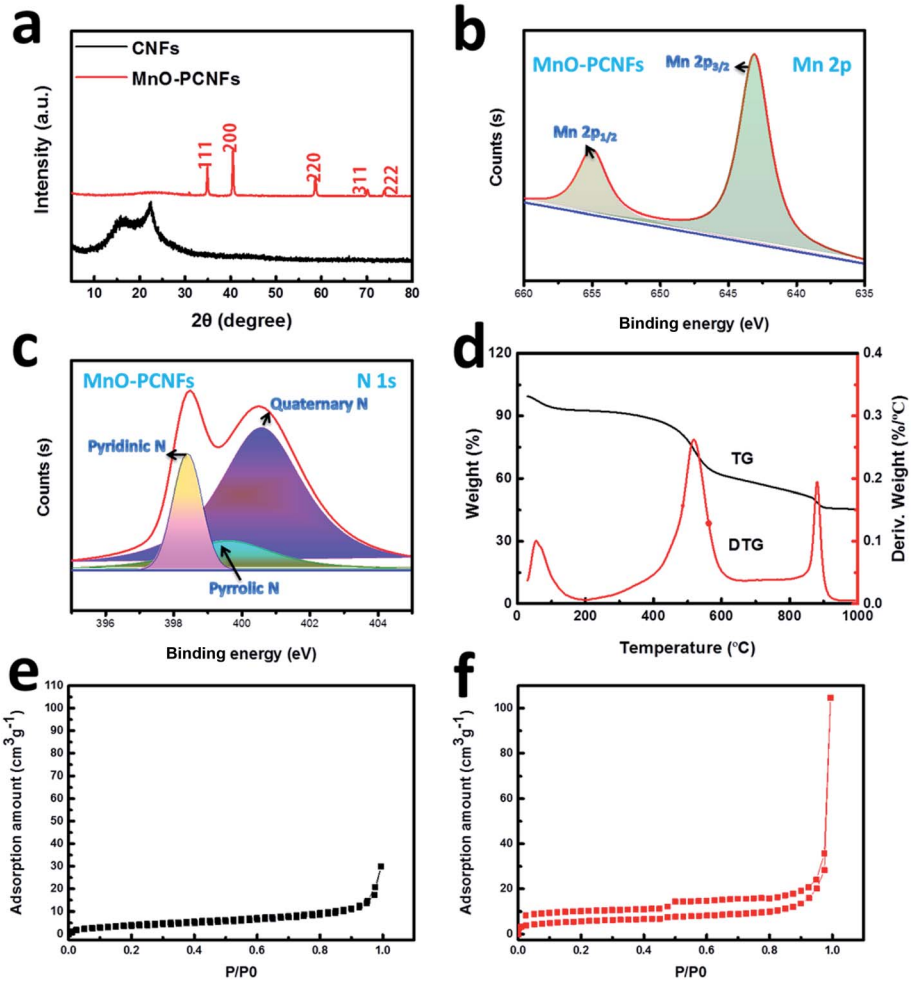


Fig. 5 (a) XRD patterns of MnO–PCNFs and CNFs. XPS spectra of the as-prepared MnO–PCNFs: (b) Mn 2p and (c) N 1s. (d) TG and DTG of MnO–PCNFs; the pristine adsorption–desorption curves of (e) CNFs and (f) MnO–PCNFs.

### 3.3 Physical properties

Outstanding electrical conductivity and large specific surface area could lower the local current density, resulting in low interfacial resistance.[26,29] Table 1 displays the electrical conductivity and specific surface area of flexible PI-based CNFs and MnO–PCNFs. The flexible PI-based CNFs exhibited a good conductivity of 663.67 S $m^{-1}$. However, the conductivity of MnO–PCNFs was 866.96 S $m^{-1}$ because their porous architecture affected the degree of graphitization during the carbonization procedure, which could facilitate the electron transport of the entire composite Li metal electrode. The large specific surface area of MnO–PCNFs offered a spatial location for the deposition of Li. In addition, the growth of Li dendrites would be overpowered under the direction of MnO seeds due to the lithiophilic feature of the N dopants and the capillary force of the porous architectures.[46] In Table 1 and Fig. 5(e and f), the surface area of flexible CNFs and MnO-PCNFs could gain 8.92 and 20.92 $m^2$ $g^{-1}$, respectively.[47] The larger surface area of MnO–PCNFs offered enough space for Li deposition, and remarkable electrical conductivity could enhance the electron transport performance of Li electrodes, which was one of the essential factors for superior electrochemical performance of the assembled cell. The advanced performance of the modified battery could be attributed to the addition of the prepared flexible PI-based MnO–PCNF interlayers. On the one hand, the flexible films with a self-support and porous skeleton with the capillary force for Li could be regarded as transitional layers to adjust the volume expansion of the Li metal and accelerate Li insertion into the interior/surface of carbon nanofibers. On the other hand, the flexible carbon nanofiber skeleton-doped MnO and N could offer more active sites to induce more adequate and uniform Li deposition and stripping.

Table 1 Electrical conductivity and surface area of CNFs and MnO–PCNFs

| Sample | Electrical conductivity (S $m^{-1}$) | BET surface area ($m^2$ $g^{-1}$) |
|---|---|---|
| CNFs | 663.67 | 8.92 |
| MnO–PCNFs (800 °C) | 866.96 | 20.92 |

### 3.4 Electrochemical cycling performance

The EIS curves were engaged to test the charge-transfer kinetics of the three modified cells. As shown in Fig. 6(a–c), the interface impedance and stability of Li–Li batteries with the prepared interlayers were explored by the EIS at 1 mA $cm^{-2}$ and 1 mA h $cm^{-2}$. The Nyquist plots of the assembled Li–Li cells were utilized to display the internal resistance of the three cells before and after the cycles (Fig. 6(a–c)). The interface resistance of the electrolyte/electrode to the charge transfer resistance of the electrode was connected with the semicircle of the high-frequency region. Before the cycle, the cells with PP and CNFs-PP showed a comparatively large interface resistance, which might be attributed to the generation of a passivation film on the anodes. After the first and tenth cycles, the interface resistance of the assembled battery always decreased,[48] which might be connected with the decomposition of the passivation film or the increase in surface area during Li dendrite generation.[27,31] By comparison, the cells with MnO–PCNFs-PP displayed a lower interfacial impedance before electrochemistry cycling, after 1 cycle and after 10 cycles. The steady interface was derived from the homogeneous dispersed nucleation and invertible dissolution of Li on MnO–PCNFs by reason of the direction of MnO seeds, the lithiophilic feature of the N dopants and the capillary force of the porous architectures, which also endowed it with remarkable electrochemical performance.[49] The prepared MnO–PCNFs presented a robust flexible architecture without binders, high specific surface area and excellent electrical conductivity, which were good for electrochemical reaction kinetics and current density near a uniform anode, resulting in low interface resistance.

The galvanostatic cycles of Li–Li cells are conducted to probe the long-time cycling stability of the anodes with the interlayer.

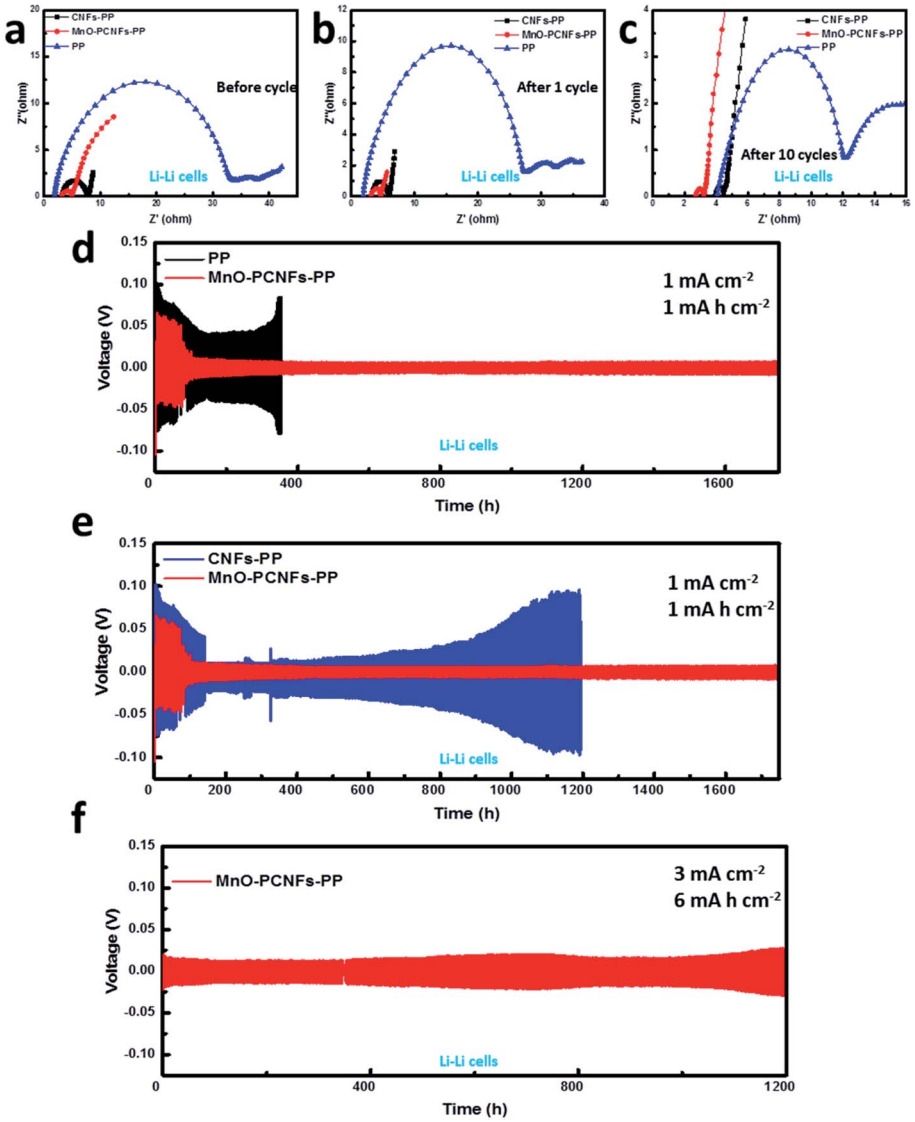


Fig. 6 EIS of the Li–Li cells (a) before cycling, (b) after 1 cycle, and (c) after 10 cycles at 1 mA $cm^{-2}$ and 1 mA h $cm^{-2}$. Voltage profile of the Li–Li cells with a separator of (d) PP and MnO–PCNFs-PP, (e) CNFs-PP and MnO–PCNFs-PP at 1 mA $cm^{-2}$ and 1 mA h $cm^{-2}$ and (f) MnO–PCNFs-PP at 3 mA $cm^{-2}$ and 6 mA h $cm^{-2}$.

Fig. 6(d and e) presents the voltage profile of the Li–Li batteries at 1 mA $cm^{-2}$ and 1 mA h $cm^{-2}$. The deposition actions of Li have an important influence on its electrochemical performance. When batteries were assembled with a PP separator, the Li metal would generate Li columns and dendrites, leading to "dead Li", which was extremely inferior to the Li anode. The results can be verified through cycling the Li anode with PP at 1 mA $cm^{-2}$ and 1 mA h $cm^{-2}$. After 353 h, an overpotential performance can be presented, which demonstrated the formation of ramose Li dendrites. For the Li–Li cells with the bare Li metal as the anode, it can be observed that the voltage rises with the growth of cycling time, which displays that the polarization phenomenon can be developed seriously in the Li deposition–stripping procedure. The tested result is the sign of the Li dendrites growing out on the Li metal anode. An alike phenomenon in the cells with CNF interlayers (1200 h) and a polarization phenomenon are extremely serious. The Li–Li cells with MnO–PCNFs-PP presented a small voltage hysteresis and a certain cycling stability when compared with pristine Li, which displayed that MnO–PCNFs can overpower the growth of Li dendrites.[34,42] As the nucleation and growth of the Li metal are induced by the prepared MnO NPs, the lithiophilic feature of the N dopants and the capillary force of the porous architectures on PCNFs, the Li metal with the interlayer can be homogeneously deposited in the PCNF material. The Li metal anode with MnO–PCNFs displayed a brilliant cycling performance at 1 mA $cm^{-2}$ for 1750 h with a small overpotential. In Fig. 6(f), the Li–Li cells assembled with MnO–PCNFs-PP can work at a high current density of 3 mA $cm^{-2}$ for 1200 h, and the voltage polarization was not greatly augmented.

MnO–PCNFs gain a flexible architecture, large specific surface area and excellent electrical conductivity, which are helpful to decrease the local current density of the lithium metal anode, leading to low interface resistance and the reduced formation of the dendrite-free Li electrode.[27,34,50] The porous architecture permitted the anode with MnO–PCNF interlayers to gain the capillary force, a richer inner hollow space and more Li loading capacity than those of CNFs.[46] Under the direction of homogeneous MnO NP seeds, the Li metal was consistently and uniformly deposited in the outer and inner channels of PCNFs.[42]

To explore the electrochemical cycling performance, PP, CNFs-PP and MnO–PCNFs-PP are engaged in Li–Cu batteries. Fig. 7(a) displays coulombic efficiencies (CE) of the Li–Cu batteries at 1 mA $cm^{-2}$ and 1 mA h $cm^{-2}$. The figure outcomes offer the other viewpoint on the growth of Li dendrites or "dead Li" during the Li deposition–stripping process. After 51 cycles, the battery with a PP separator displayed an uneven striping procedure, while the battery with MnO–PCNFs-PP showed a steady striping shape. The rapid falling-off in the deposition/striping procedure corresponding to the CE falls to 0% after 51 cycles in the battery with a pristine PP separator. In contrast, a steady CE of 97% after 200 cycles could be retained with the assembled cell with MnO–PCNFs-PP. The Li–Cu battery with CNFs-PP is similar to the Li–Cu battery with PP. In Fig. 7(b), the Li–Cu batteries with MnO–PCNFs-PP at 3 mA $cm^{-2}$ and 3 mA h $cm^{-2}$ were steady, and the CE was sustained at around 80% after 200 cycles. In conclusion, the electrochemical performance of Li–Cu cells with MnO–PCNFs-PP was significantly enhanced because of the affinity of inserted MnO with Li, the lithiophilic feature of the N dopants and the capillary strength of the porous architectures. The overhead results exhibited that the cycling performance of the Li metal anode at equal current densities was meaningfully enhanced with the applied MnO–PCNFs-PP. The obtained pores endowed the MnO–PCNFs with the lithiophilic characteristic, sufficient internal space and excellent Li loading capacity.[46] All of these results indicated that MnO–PCNFs can be regarded as interlayer materials for the deposition of Li, which mainly resolved the dendrite puzzler.

Lithium–sulfur (Li–S) batteries were used to test the cycling performance of the full-cell with the prepared interlayer. The EIS of the Li–S batteries was utilized to survey the charge transfer kinetics. Fig. 7(c and d) show the typical Nyquist plots of the batteries with PP, CNFs-PP and MnO–PCNFs before cycle and after 5 cycles. The Nyquist plot is semi-circular at high frequencies and slanting at low frequencies, corresponding to the oblique lines of ion diffusion.[51] The batteries with PP and CNFs-PP deliver larger semicircular diameters than that of the batteries with MnO–PCNFs-PP, which illustrates that the batteries with PP and CNFs-PP display a higher charge-transfer resistance than the batteries with MnO–PCNFs-PP.[52] The slant of the diagonal mark is large, which means that the Warburg impedance of the batteries is low. In Fig. 7(c), the Warburg impedance of the batteries with MnO–PCNFs-PP is smaller than those of the cells with PP and CNFs-PP, which is advantageous for the transportation of $Li^+$. The decrease in Warburg's impedance can be put down to the outstanding conductive net architecture of the MnO–PCNFs.[34,53–56] The impedance spectra demonstrated that two semicircles were present after 5 cycles for these batteries, as shown in Fig. 7(d). The arrival of the second semicircle is attributed to the creation of $Li_2S$ and $Li_2S_2$ during electrochemical cycling. As presented in Fig. 7(d), these batteries after 5 cycles displayed clearly reduced resistances compared with the corresponding fresh batteries. The reduced impedance was attributed to the natural arrangement of Li during the stripping-plating process because of the affinity of inserted MnO with Li, the lithiophilic feature of the N dopants and the capillary strength of the porous architectures, which held a more beneficial electrochemical site,[57] suggesting a closer interaction and better coverage between the Li metal and MnO–PCNFs.[58]

The cycling performance of the Li–S batteries at 1C was researched, as presented in Fig. 7(e). The discharge capacity of the battery with MnO–PCNFs-PP was much higher and steadier than those of the batteries with PP and CNFs-PP. In addition, it was revealed that the batteries with PP, CNFs-PP and MnO–PCNFs-PP exhibited initial discharge capacities of 551.3, 735 and 730 mA h $g^{-1}$, respectively. The discharge capacity of the batteries with PP, CNFs-PP, MnO–PCNFs-PP was reserved at 370.7, 624.3 and 710.3 mA h $g^{-1}$ after 200 cycles, respectively. After 500 cycles, the batteries with PP cannot work in the required capacity and the capacity of the batteries with CNFs-PP and MnO–PCNFs-PP remained at 473.7 and 601.2 mA h $g^{-1}$,

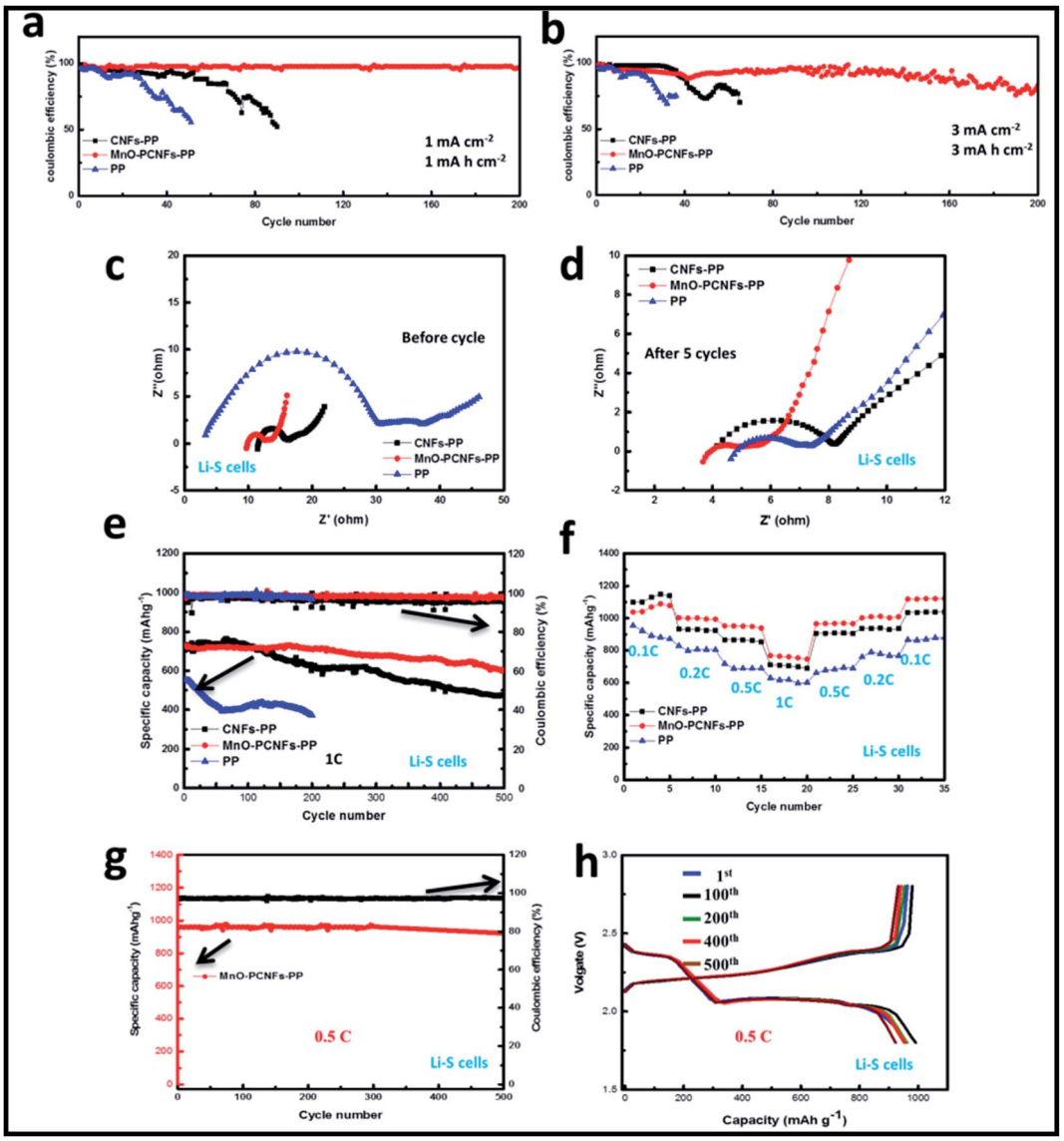


Fig. 7 (a) Coulombic efficiencies of the Li–Cu cells at 1 mA $cm^{-2}$ and 1 mA h $cm^{-2}$. (b) Coulombic efficiencies of the Li–Cu cells at 3 mA $cm^{-2}$ and 3 mA h $cm^{-2}$. The EIS (c) before cycle and (d) after 5 cycles of the Li–S cells. (e) Discharge capacity and CE of the Li–S cells at 1C. (f) Rate performance of the Li–S cells. (g) Discharge capacity and CE at 0.5C of the Li–S cells with MnO–PCNFs-PP and (h) the corresponding charge–discharge curves of MnO–PCNFs-PP at 0.5C.

respectively. The Li–S batteries with MnO–PCNFs displayed an outstanding rate performance (Fig. 7(f)). The discharge capacity of the batteries with the prepared MnO–PCNFs can obtain 1038.2, 1002.7, 952, 768.4, 966.2, 1002.3 and 1118.7 mA h $g^{-1}$ with current densities of 0.1, 0.2, 0.5, 1, 0.5, 0.2 and 0.1C. While the batteries with CNFs can obtain 1098.2, 932.7, 867, 712.4, 906.2, 937.3, and 1035.7 mA h $g^{-1}$, respectively. In addition, the discharge capacity of the cells with PP was the lowest. The Li–S batteries with MnO–PCNFs at 0.5C are shown in Fig. 7(g). The discharge capacity remained at 922.5 mA h $g^{-1}$ after 500 cycles (with a CE of about 97.82 wt%), obtaining a capacity retention rate of 96.34%. Fig. 7(h) shows the constant current charge and discharge curves of the Li–S cells with MnO–PCNFs-PP at 0.5C. After the 1st, 100th, 200th, 400th and 500th cycles, the charge and discharge curves of the Li–S cells with MnO–PCNFs-PP presented the smallest alteration, demonstrating that the Li metal anode with MnO–PCNFs obtained excellent cycle retention.

### 3.5 Morphological evolution

As presented in Fig. 8(a), the probable mechanisms of flexible MnO–PCNFs as interlayers for Li metal batteries are clarified as follows: first, PCNFs with a flexible property, large specific surface area and outstanding conductivity as interlayers in Li metal cells could offer more space and build a great electronic transmission network to prompt more adequate and uniform Li deposition and stripping. The capillary power of the porous skeletons conduces to increase the splendid Li wettability of the MnO–PCNF interlayers, and the flexible architecture is helpful

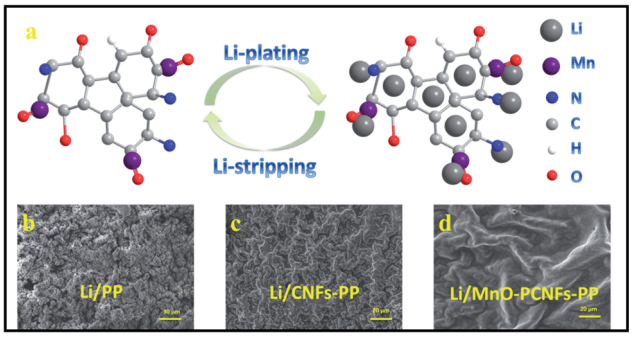


Fig. 8 (a) Schematic of the Li stripping-plating process on PI-based flexible MnO–PCNFs. Surface SEM images of the Li-metal electrode with (b) PP (c) CNFs-PP and (d) MnO–PCNFs-PP. The electrodes were obtained from the Li–Li cells cycled for 200 h at 1 mA $cm^{-2}$ and 1 mA h $cm^{-2}$.

to accommodate the volume alteration of the Li metal anode during the stripping–plating process.[15] Second, the flexible films with *in situ* doped MnO nanoparticles can obtain effective force with Li during the Li deposition–stripping procedure. The Mn-based metal oxides can combine with $Li^+$ to generate an analogous alloy reaction during the Li deposition–stripping procedure. The Li can be homogeneously dispersed in the interior or the surface of PCNFs to hold up the huge accretion of the Li metal.[16] During the initial time of the Li plating procedure, it is speculated that $Li^+$ favors the nucleation on the MnO seeds with the following reaction: $Li^+ + MnO \rightarrow Li_2O + Mn$. With the further plating, the Li metal could be alloyed with MnO to generate LiMn (Li + Mn → LiMn).[15,59] Third, the doped N in the prepared PCNFs could greatly accelerate the nucleation of Li on PCNFs by the significantly reduced nucleation energy barrier, which are good for the saturation of the electrolyte and can offer more active sites to insert/extract Li.[45,60]

The lithium metal anode after the cycle was examined by SEM to explore the "geographical" distribution of the deposited Li metal anode. Fig. 8(b–d) show the surface morphological architectures of the Li metal anode with PP, CNFs-PP and MnO–PCNFs-PP. The Li–Li batteries were tested at 1 mA $cm^{-2}$ and 1 mA h $cm^{-2}$ for 200 h. The surface of the fresh Li metal anode was homogeneous on the whole except for a few minor flaws. As displayed in Fig. 8(b), the surface of the bare Li metal anode became uneven, and there were numerous accidental movable pores, in which Li bars were noticeable. The Li bars finally came into the Li dendrite and pierced the separator, leading to a short circuit. As presented in Fig. 8(c), the surface of Li metal anodes with CNFs-PP turned to be coarse and the Li metal developed to be particles and partial pieces. The surface of the Li metal anode was more close-grained and tabular than that of Li metal anode with PP. The total morphologies of Fig. 8(c) were that the particles were interphase with flat Li pieces. By comparison, the Li metal anode with MnO–PCNFs-PP was flat with rare pore and reduced dendrite architectures, as shown in Fig. 8(d), which was because MnO–PCNFs effectively controlled Li development in space when compared to others (Fig. 8(b and c)).[46,61] Consequently, the creation of Li dendrites was hindered and the growth vigour of dendrites was cut down in Fig. 8(d).

# 4. Conclusions

In summary, original flexible MnO–PCNF interlayers have been successfully synthesized by an electrospinning and carbonization technology. The prepared MnO–PCNF interlayers exhibited many merits such as the affinity feature of inserted MnO with Li, the lithiophilic characteristic of N dopants and the capillary power of porous architectures. Furthermore, flexible skeletons without binders of the obtained MnO–PCNFs can be well retained during the Li deposition–stripping procedure, and they can offer a depositional carrier for homogenously deposited Li and fast charge transfer for Li redox reactions. Particularly, the prepared MnO–PCNF interlayers with an outstanding stable and flexible structure, large specific surface area and preeminent electrical conductivity can accommodate volume change, homogenize the current density, and hinder the growth of Li dendrites. Therefore, the Li metal anode with MnO–PCNF interlayers displays prominent electrochemical performance with a low overpotential of 1 mA $cm^{-2}$ and a long lifetime up to 1750 h. When assembled with the interlayer, the Li metal anode in the Li–S cell with MnO–PCNF interlayers shows great specific capacity, cycling stability and rate performance. This work will enlighten a novel path to attain steady Li metal anodes for high-areal-capacity cells and offer chances for the application of MnO–PCNF materials toward superior Li metal anodes.

# Conflicts of interest

The authors declare no competing financial interest.

# Acknowledgements

This study was supported by the National Natural Science Foundation of China (51973157), the Science, Technology Plans of Tianjin (17PTSYJC00040, 18PTSYJC00180) and the Natural Science Foundation of Tianjin City (17JCYBJC41700), Scientific Research Project of Tianjin Municipal Education Commission (2017KJ067) and Tianjin Scientific Research Foundation for the Returned Overseas Chinese Scholars (2018003).

# References

1 F. Guo, T. Kang, Z. Liu, B. Tong, L. Guo, Y. Wang, C. Liu, X. Chen, Y. Zhao, Y. Shen, W. Lu, L. Chen and Z. Peng, Advanced Lithium Metal-Carbon Nanotube Composite Anode for High-Performance Lithium-Oxygen Batteries, *Nano Lett.*, 2019, 6377–6384.

2 F. Zhao, X. Zhou, W. Deng and Z. Liu, Entrapping lithium deposition in lithiophilic reservoir constructed by vertically aligned ZnO nanosheets for dendrite-free Li metal anodes, *Nano Energy*, 2019, **62**, 55–63.

3 H. Fan, Q. Dong, C. Gao, B. Hong, Z. Zhang, K. Zhang and Y. Lai, Encapsulating Metallic Lithium into Carbon Nanocages Which Enables a Low-Volume Effect and a Dendrite-Free Lithium Metal Anode, *ACS Appl. Mater. Interfaces*, 2019, **11**(34), 30902–30910.

4 C. Niu, H. Pan, W. Xu, J. Xiao, J. G. Zhang, L. Luo, C. Wang, D. Mei, J. Meng, X. Wang, Z. Liu, L. Mai and J. Liu, Self-smoothing anode for achieving high-energy lithium metal batteries under realistic conditions, *Nat. Nanotechnol.*, 2019, **14**(6), 594–601.

5 X. B. Cheng, R. Zhang, C. Z. Zhao and Q. Zhang, Toward Safe Lithium Metal Anode in Rechargeable Batteries: A Review, *Chem. Rev.*, 2017, **117**(15), 10403–10473.

6 X. B. Cheng, M. Q. Zhao, C. Chen, A. Pentecost, K. Maleski, T. Mathis, X. Q. Zhang, Q. Zhang, J. Jiang and Y. Gogotsi, Nanodiamonds suppress the growth of lithium dendrites, *Nat. Commun.*, 2017, **8**(1), 336.

7 X. Judez, H. Zhang, C. Li, G. G. Eshetu, J. A. Gonzalez-Marcos, M. Armand and L. M. Rodriguez-Martinez, Review-Solid Electrolytes for Safe and High Energy Density Lithium-Sulfur Batteries: Promises and Challenges, *J. Electrochem. Soc.*, 2018, **165**(1), A6008–A6016.

8 W. Li, H. Yao, K. Yan, G. Zheng, Z. Liang, Y. M. Chiang and Y. Cui, The synergetic effect of lithium polysulfide and lithium nitrate to prevent lithium dendrite growth, *Nat. Commun.*, 2015, **6**, 7436.

9 X.-Q. Zhang, X.-B. Cheng, X. Chen, C. Yan and Q. Zhang, Fluoroethylene Carbonate Additives to Render Uniform Li Deposits in Lithium Metal Batteries, *Adv. Funct. Mater.*, 2017, **27**(10), 1605989.

10 F. Ding, W. Xu, G. L. Graff, J. Zhang, M. L. Sushko, X. Chen, Y. Shao, M. H. Engelhard, Z. Nie, J. Xiao, X. Liu, P. V. Sushko, J. Liu and J. G. Zhang, Dendrite-free lithium deposition via self-healing electrostatic shield mechanism, *J. Am. Chem. Soc.*, 2013, **135**(11), 4450–4456.

11 H.-L. Wu, M. Shin, Y.-M. Liu, K. A. See and A. A. Gewirth, Thiol-based electrolyte additives for high-performance lithium-sulfur batteries, *Nano Energy*, 2017, **32**, 50–58.

12 J. Zheng, M. Gu, H. Chen, P. Meduri, M. H. Engelhard, J.-G. Zhang, J. Liu and J. Xiao, Ionic liquid-enhanced solid state electrolyte interface (SEI) for lithium–sulfur batteries, *J. Mater. Chem. A*, 2013, **1**(29), 8464.

13 Y. Liu, D. Lin, P. Y. Yuen, K. Liu, J. Xie, R. H. Dauskardt and Y. Cui, An Artificial Solid Electrolyte Interphase with High Li-Ion Conductivity, Mechanical Strength, and Flexibility for Stable Lithium Metal Anodes, *Adv. Mater.*, 2017, **29**(10), 1605531.

14 H. Zhai, P. Xu, M. Ning, Q. Cheng, J. Mandal and Y. Yang, A Flexible Solid Composite Electrolyte with Vertically Aligned and Connected Ion-Conducting Nanoparticles for Lithium Batteries, *Nano Lett.*, 2017, **17**(5), 3182–3187.

15 G. Jiang, N. Jiang, N. Zheng, X. Chen, J. Mao, G. Ding, Y. Li, F. Sun and Y. Li, MOF-derived porous $Co_3O_4$-NC nanoflake arrays on carbon fiber cloth as stable hosts for dendrite-free Li metal anodes, *Energy Storage Mater.*, 2019, 181–189.

16 Y. Liu, S. Zhang, X. Qin, F. Kang, G. Chen and B. Li, In-Plane Highly Dispersed $Cu_2O$ Nanoparticles for Seeded Lithium Deposition, *Nano Lett.*, 2019, **19**(7), 4601–4607.

17 C. Guo, H. Yang, A. Naveed, Y. Nuli, J. Yang, Y. Cao, H. Yang and J. Wang, $AlF_3$-Modified carbon nanofibers as a multifunctional 3D interlayer for stable lithium metal anodes, *Chem. Commun.*, 2018, **54**(60), 8347–8350.

18 Z. Liang, G. Zheng, C. Liu, N. Liu, W. Li, K. Yan, H. Yao, P. C. Hsu, S. Chu and Y. Cui, Polymer nanofiber-guided uniform lithium deposition for battery electrodes, *Nano Lett.*, 2015, **15**(5), 2910–2916.

19 G. Zheng, S. W. Lee, Z. Liang, H. W. Lee, K. Yan, H. Yao, H. Wang, W. Li, S. Chu and Y. Cui, Interconnected hollow carbon nanospheres for stable lithium metal anodes, *Nat. Nanotechnol.*, 2014, **9**(8), 618–623.

20 Q. Pang, A. Shyamsunder, B. Narayanan, C. Y. Kwok, L. A. Curtiss and L. F. Nazar, Tuning the electrolyte network structure to invoke quasi-solid state sulfur conversion and suppress lithium dendrite formation in Li-S batteries, *Nat. Energy*, 2018, **3**(9), 783–791.

21 D. Lin, Y. Liu, Z. Liang, H.-W. Lee, J. Sun, H. Wang, K. Yan, J. Xie and Y. Cui, Layered reduced graphene oxide with nanoscale interlayer gaps as a stable host for lithium metal anodes, *Nat. Nanotechnol.*, 2016, **11**(7), 626–632.

22 H. Lee, J. Song, Y.-J. Kim, J.-K. Park and H.-T. Kim, Structural modulation of lithium metal-electrolyte interface with three-dimensional metallic interlayer for high-performance lithium metal batteries, *Sci. Rep.*, 2016, **6**, 30830.

23 C. Wang, K. R. Adair, J. Liang, X. Li, Y. Sun, X. Li, J. Wang, Q. Sun, F. Zhao, X. Lin, R. Li, H. Huang, L. Zhang, R. Yang, S. Lu and X. Sun, Solid-State Plastic Crystal Electrolytes: Effective Protection Interlayers for Sulfide-Based All-Solid-State Lithium Metal Batteries, *Adv. Funct. Mater.*, 2019, **29**(26), 1900392.

24 Y. Deng, H. Lu, Y. Cao, B. Xu, Q. Hong, W. Cai and W. Yang, Multi-walled carbon nanotube interlayers with controllable thicknesses for high-capacity and long-life lithium metal anodes, *J. Power Sources*, 2019, **412**, 170–179.

25 T. Pakki, E. H. Mohan, N. Y. Hebalkar, J. Adduru, S. V. Bulusu, A. Srinivasan, K. M. Mantravadi and N. R. Tata, Flexible and free-standing carbon nanofiber matt derived from electrospun polyimide as an effective interlayer for high-performance lithium-sulfur batteries, *J. Mater. Sci.*, 2019, **54**(12), 9075–9087.

26 M. Liu, N. Deng, J. Ju, L. Fan, L. Wang, Z. Li, H. Zhao, G. Yang, W. Kang, J. Yan and B. Cheng, A Review: Electrospun Nanofiber Materials for Lithium-Sulfur Batteries, *Adv. Funct. Mater.*, 2019, 1905467.

27 Q. Qin, N. Deng, L. Wang, L. Zhang, Y. Jia, Z. Dai, Y. Liu, W. Kang and B. Cheng, Novel flexible Mn-based carbon nanofiber films as interlayers for stable lithium-metal battery, *Chem. Eng. J.*, 2019, **360**, 900–911.

28 B. Maharjan, M. K. Joshi, A. P. Tiwari, C. H. Park and C. S. Kim, In-situ synthesis of AgNPs in the natural/synthetic hybrid nanofibrous scaffolds: Fabrication, characterization and antimicrobial activities, *J. Mech. Behav. Biomed. Mater.*, 2017, **65**, 66–76.

29 M. Liu, N. Deng, J. Ju, L. Wang, G. Wang, Y. Ma, W. Kang and J. Yan, Silver Nanoparticle-Doped 3D Porous Carbon Nanofibers as Separator Coating for Stable Lithium Metal Anodes, *ACS Appl. Mater. Interfaces*, 2019, 17843–17852.

30 K. Yan, Z. Lu, H.-W. Lee, F. Xiong, P.-C. Hsu, Y. Li, J. Zhao, S. Chu and Y. Cui, Selective deposition and stable

encapsulation of lithium through heterogeneous seeded growth, *Nat. Energy*, 2016, **1**(3), 16010.

31 Q. Li, S. Zhu and Y. Lu, 3D Porous Cu Current Collector/Li-Metal Composite Anode for Stable Lithium-Metal Batteries, *Adv. Funct. Mater.*, 2017, **27**(18), 1606422.

32 J. Pu, J. Li, Z. Shen, C. Zhong, J. Liu, H. Ma, J. Zhu, H. Zhang and P. V. Braun, Interlayer Lithium Plating in Au Nanoparticles Pillared Reduced Graphene Oxide for Lithium Metal Anodes, *Adv. Funct. Mater.*, 2018, **28**(41), 1804133.

33 H.-K. Kang, S.-G. Woo, J.-H. Kim, J.-S. Yu, S.-R. Lee and Y.-J. Kim, Few-Layer Graphene Island Seeding for Dendrite-Free Li Metal Electrodes, *ACS Appl. Mater. Interfaces*, 2016, **8**(40), 26895–26901.

34 R. Zhang, X. Chen, X. Shen, X.-Q. Zhang, X.-R. Chen, X.-B. Cheng, C. Yan, C.-Z. Zhao and Q. Zhang, Coralloid Carbon Fiber-Based Composite Lithium Anode for Robust Lithium Metal Batteries, *Joule*, 2018, **2**(4), 764–777.

35 J. Cui, S. Yao, M. Ihsan-Ul-Haq, J. Wu and J.-K. Kim, Correlation between Li Plating Behavior and Surface Characteristics of Carbon Matrix toward Stable Li Metal Anodes, *Adv. Energy Mater.*, 2019, **9**(1), 1802777.

36 A. Schneider, C. Suchomski, H. Sommer, J. Janek and T. Brezesinski, Free-standing and binder-free highly N-doped carbon/sulfur cathodes with tailorable loading for high-areal-capacity lithium–sulfur batteries, *J. Mater. Chem. A*, 2015, **3**(41), 20482–20486.

37 S. Tao, B. Li, J. Zhang, P. Cui, D. Wu, W. Chu, B. Qian and L. Song, In situ synthesis of ultrasmall MnO nanoparticles encapsulated by a nitrogen-doped carbon matrix for high-performance lithium-ion batteries, *Chem. Commun.*, 2019, **55**(62), 9184–9187.

38 F. Liang, L. Lin, Z. Feng, C. Chu, J. Pan, J. Yang and Y. Qian, Spatial separation of lithiophilic surface and superior conductivity for advanced Li metal anode: the case of acetylene black and N-doped carbon spheres, *J. Mater. Chem. A*, 2019, **7**(15), 8765–8770.

39 H. Wu, Y. Zhang, Y. Deng, Z. Huang, C. Zhang, Y.-B. He, W. Lv and Q.-H. Yang, A lightweight carbon nanofiber-based 3D structured matrix with high nitrogen-doping level for lithium metal anodes, *Sci. China Mater.*, 2018, **62**(1), 87–94.

40 X. Chen, L. Yuan, Z. Hao, X. Liu, J. Xiang, Z. Zhang, Y. Huang and J. Xie, Free-Standing $Mn_3O_4$@CNF/S Paper Cathodes with High Sulfur Loading for Lithium-Sulfur Batteries, *ACS Appl. Mater. Interfaces*, 2018, **10**(16), 13406–13412.

41 K. Kadirvelu and N. N. Fathima, Self-assembly of keratin peptides: its implication on the performance of electrospun PVA nanofibers, *Sci. Rep.*, 2016, **6**(1), 36558.

42 C. Yang, Y. Yao, S. He, H. Xie, E. Hitz and L. Hu, Ultrafine Silver Nanoparticles for Seeded Lithium Deposition toward Stable Lithium Metal Anode, *Adv. Mater.*, 2017, **29**(38), 1702714.

43 R. Liu, X. Chen, C. Zhou, A. Li, Y. Gong, N. Muhammad and H. Song, Controlled synthesis of porous 3D interconnected MnO/C composite aerogel and their excellent lithium-storage properties, *Electrochim. Acta*, 2019, **306**, 143–150.

44 M. Gao, S. Huang, Q. Zhang, G. Xu, Z. Chen, Y. Xiao, L. Yang, J. Cao and X. Wei, Hierarchically Pomegranate-Like MnO@porous Carbon Microspheres as an Enhanced-Capacity Anode for Lithium-Ion Batteries, *ChemElectroChem*, 2019, **6**(11), 2891–2900.

45 S. Huang, L. Yang, M. Gao, Q. Zhang, G. Xu, X. Liu, J. Cao and X. Wei, Well-dispersed MnO-quantum-dots/N-doped carbon layer anchored on carbon nanotube as free-standing anode for high-performance Li-Ion batteries, *Electrochim. Acta*, 2019, **319**, 302–311.

46 J. Xiang, Y. Zhao, L. Yuan, C. Chen, Y. Shen, F. Hu, Z. Hao, J. Liu, B. Xu and Y. Huang, A strategy of selective and dendrite-free lithium deposition for lithium batteries, *Nano Energy*, 2017, **42**, 262–268.

47 J. Ju, W. Kang, N. Deng, L. Li, Y. Zhao, X. Ma, L. Fan and B. Cheng, Preparation and characterization of PVA-based carbon nanofibers with honeycomb-like porous structure via electro-blown spinning method, *Microporous Mesoporous Mater.*, 2017, **239**, 416–425.

48 N. Deng, W. Kang, J. Ju, L. Fan, X. Zhuang, X. Ma, H. He, Y. Zhao and B. Cheng, Polyvinyl Alcohol-derived carbon nanofibers/carbon nanotubes/sulfur electrode with honeycomb-like hierarchical porous structure for the stable-capacity lithium/sulfur batteries, *J. Power Sources*, 2017, **346**, 1–12.

49 T. T. Zuo, X. W. Wu, C. P. Yang, Y. X. Yin, H. Ye, N. W. Li and Y. G. Guo, Graphitized Carbon Fibers as Multifunctional 3D Current Collectors for High Areal Capacity Li Anodes, *Adv. Mater.*, 2017, **29**(29), 1700389.

50 J. Hu, K. Chen and C. Li, Nanostructured Li-Rich Fluoride Coated by Ionic Liquid as High Ion-Conductivity Solid Electrolyte Additive to Suppress Dendrite Growth at Li Metal Anode, *ACS Appl. Mater. Interfaces*, 2018, **10**(40), 34322–34331.

51 G. Zhou, S. Pei, L. Li, D.-W. Wang, S. Wang, K. Huang, L.-C. Yin, F. Li and H.-M. Cheng, A Graphene-Pure-Sulfur Sandwich Structure for Ultrafast, Long-Life Lithium-Sulfur Batteries, *Adv. Mater.*, 2014, **26**(4), 625–631.

52 S. Niu, W. Lv, C. Zhang, Y. Shi, J. Zhao, B. Li, Q.-H. Yang and F. Kang, One-pot self-assembly of graphene/carbon nanotube/sulfur hybrid with three dimensionally interconnected structure for lithium–sulfur batteries, *J. Power Sources*, 2015, **295**, 182–189.

53 L. Tan, X. Li, Z. Wang, H. Guo, J. Wang and L. An, Multifunctional Separator with Porous Carbon/Multi-Walled Carbon Nanotube Coating for Advanced Lithium–Sulfur Batteries, *ChemElectroChem*, 2018, **5**(1), 71–77.

54 H. J. Peng, D. W. Wang, J. Q. Huang, X. B. Cheng, Z. Yuan, F. Wei and Q. Zhang, Janus Separator of Polypropylene-Supported Cellular Graphene Framework for Sulfur Cathodes with High Utilization in Lithium-Sulfur Batteries, *Adv. Sci.*, 2016, **3**(1), 1500268.

55 J. Balach, H. K. Singh, S. Gomoll, T. Jaumann, M. Klose, S. Oswald, M. Richter, J. Eckert and L. Giebeler, Synergistically Enhanced Polysulfide Chemisorption Using a Flexible Hybrid Separator with N and S Dual-Doped Mesoporous Carbon Coating for Advanced Lithium-Sulfur

Batteries, *ACS Appl. Mater. Interfaces*, 2016, **8**(23), 14586–14595.

56 Z. Zhang, Y. Lai, Z. Zhang, K. Zhang and J. Li, $Al_2O_3$-coated porous separator for enhanced electrochemical performance of lithium sulfur batteries, *Electrochim. Acta*, 2014, **129**, 55–61.

57 L. Zeng, F. Pan, W. Li, Y. Jiang, X. Zhong and Y. Yu, Free-standing porous carbon nanofibers-sulfur composite for flexible Li-S battery cathode, *Nanoscale*, 2014, **6**(16), 9579–9587.

58 Z. Li, C. Li, X. Ge, J. Ma, Z. Zhang, Q. Li, C. Wang and L. Yin, Reduced graphene oxide wrapped MOFs-derived cobalt-doped porous carbon polyhedrons as sulfur immobilizers as cathodes for high performance lithium sulfur batteries, *Nano Energy*, 2016, **23**, 15–26.

59 C. Jin, O. Sheng, J. Luo, H. Yuan, C. Fang, W. Zhang, H. Huang, Y. Gan, Y. Xia, C. Liang, J. Zhang and X. Tao, 3D lithium metal embedded within lithiophilic porous matrix for stable lithium metal batteries, *Nano Energy*, 2017, **37**, 177–186.

60 W. Cai, G. Li, D. Luo, G. Xiao, S. Zhu, Y. Zhao, Z. Chen, Y. Zhu and Y. Qian, The Dual-Play of 3D Conductive Scaffold Embedded with Co, N Codoped Hollow Polyhedra toward High-Performance Li-S Full Cell, *Adv. Energy Mater.*, 2018, **8**(34), 1802561.

61 V.-C. Ho, D. T. Ngo, H. T. T. Le, R. Verma, H.-S. Kim, C.-N. Park and C.-J. Park, Effect of an organic additive in the electrolyte on suppressing the growth of Li dendrites in Li metal-based batteries, *Electrochim. Acta*, 2018, **279**, 213–223.